

T. Perkins, R. Sundberg, J. Cordell, Z. Tun, and M. Owen, Real-time Target Motion Animation for Missile Warning System Testing, Proc. SPIE Vol 6208, Kissimmee, Florida, April 2006.

Copyright 2006 Society of Photo-Optical Instrumentation Engineers. One print or electronic copy may be made for personal use only. Systematic reproduction and distribution, duplication of any material in this paper for a fee or for commercial purposes, or modification of the content of the paper are prohibited.

<http://dx.doi.org/10.1117/12.661261>

See next page.

# Real-time target motion animation for missile warning system testing

Timothy Perkins\*<sup>a</sup>, Robert Sundberg<sup>a</sup>, John Cordell<sup>b</sup>, Zaw Tun<sup>b</sup>, Mark Owen<sup>b</sup>

<sup>a</sup>Spectral Sciences, Inc., Burlington MA, USA

<sup>b</sup>ACETEF, Naval Air Station, Patuxent River, MA, USA

## ABSTRACT

The QUick Image Display (QUID) model accurately computes and displays radiance images of aircraft and other objects, generically called targets, at animation rates while the target undergoes unrestricted flight. Animation rates are obtained without sacrificing radiometric accuracy by using two important innovations. First, QUID has been implemented using the Open Scene Graph (OSG) library, an open-source, cross-platform 3-D graphics toolkit for the development of high performance graphics applications in the fields of visual simulation, virtual reality, scientific visualization and modeling. Written entirely in standard C++ and fully encapsulating OpenGL and its extensions, OSG exploits modern graphics hardware to perform the computationally intensive calculations such as hidden surface removal, 3-D transformations, and shadow casting. Second, a novel formulation for reflective/emissive terms enables rapid and accurate calculation of per-vertex radiance. The bi-directional reflectance distribution function (BRDF) is decomposed into separable spectral and angular functions. The spectral terms can be pre-calculated for a user specified band pass and for a set of target-observer ranges. The only BRDF calculations which must be performed during target motion involves the observer-target-source angular functions. QUID supports a variety of target geometry files and is capable of rendering scenes containing high level-of-detail targets with thousands of facets. QUID generates accurate visible to LWIR radiance maps, in-band and spectral signatures. The newest features of QUID are illustrated with radiance and apparent temperature images of threat missiles as viewed by an aircraft missile warning system.

**Keywords:** Real-time, Scene Simulation, Infrared, Visible, Animation, Reflectance, Emission, Signature

## 1. INTRODUCTION

Missile Warning Systems (MWS) are used to warn aircraft of threat missile approach by detecting radiation associated with the rocket motor plume. Employed on helicopters, transport, reconnaissance, and attack aircraft MWS warn of threat missile approach, enabling the effective employment of evasive maneuvers and electronic and/or infrared countermeasures. Detection algorithms are used to discriminate against non-approaching radiation sources, such as glints from man-made materials or water and solar illuminated clouds. The performance of MWS has been improved through advanced image detection algorithms, and by increasing the number of spectral bands from one to two, three, or more spectral wavebands to improve false alarm mitigation and target detection. Rapid and accurate IR scene simulation, without restrictions on target location, target motion or observer motion, is a necessary factor for realistic testing of these systems in a controlled hardware-in-the-loop (HWIL) environment.

This paper examines the QUick Image Display (QUID)<sup>1-3</sup> application and its features and utility for supporting the testing of infrared sensor systems at the Air Combat Environment Test and Evaluation Facility (ACETEF) at the Naval Air Station (NAS) in Patuxent River, Maryland. Part of ACETEF's mission is to conduct ground testing of infrared sensor systems in order to improve the effectiveness of subsequent flight testing. The QUID application is one of several modeling and analysis tools used at ACETEF to provide realistic, radiometrically correct software graphics scene elements of missile hard-bodies with plumes. The scene elements can be used standalone, or built into combat scenarios for injection or infrared projection into warning and tracking sensors of installed sensor systems. The projectors used at ACETEF are either resistive arrays or digital mirror based, but in this paper they will be referred to collectively as emitters.

\*tperkins@spectral.com; phone: 781 273 4770; fax: 781 270 116; www.spectral.com

It is a major challenge to develop the software capability to provide real-time scene generation with unrestricted motion without severely degrading image content or sacrificing radiometric accuracy. The QUID model, which accurately computes and displays visible to LWIR radiance images of targets at animation rates, was recently updated to run on multiple platforms (Windows, Linux, and IRIX) and an improved user interface was implemented for added flexibility. Real-time simulation rates are attained using optimized graphics library and hardware functions to perform the more time-consuming aspects of the calculations, such as pixel filling and hidden surface calculations. In addition to utilizing the hardware of a workstation to perform the 3-D geometry computations, it is also necessary to reformulate signature calculations to perform a large fraction of the radiance calculation prior to display, allowing the graphics hardware to be fully utilized. QUID achieves fast and accurate emissivity and reflectance calculations through a novel separation of wavelength- or waveband-dependent quantities from the angular dependence, which provides the basis for the accelerated radiance calculations needed for real-time scene generation. Bandpass quantities are pre-computed by factorization of the directional emittance and a partial factorization of the bi-directional reflectance distribution function (BRDF) into functions of wavelength and functions of target, observer and light source orientations. This approach is consistent with the BRDF properties of actual materials, and makes explicit use of the mathematical structure of these validated physical models. Computational speed thus is obtained not by approximations but by reorganizing the calculations to fully utilize graphics hardware.

The inputs into QUID are standard wire-frame formats from SPIRITS<sup>4</sup>, OpenFlight<sup>5</sup>, or generic 3-D models of varying degrees of fidelity, radiometrically attributed surface and plume properties, and trajectory information. Several forms of outputs can be obtained from QUID, including streams of two-dimensionally rendered scenes with pixilated radiometry, or files of radiometrically-attributed polygons ready for scene rendering. The inputs provided and the outputs selected depend on the sensor test of interest. Key technical details of the simulation approach and recent improvements are given in the following sections. First the physical basis of the QUID simulation model is examined, then the spectral content of the images are assessed. Scaling of the pixel-based radiometric data is also analyzed, and a discussion of radiometry is provided. A complete test run of QUID is provided to show end-to-end performance.

## 2. THE QUID SIMULATION MODEL

The QUID model can generate visible through LWIR radiance maps, in-band and spectral signatures at animation rates. In a typical execution of a scene simulator, several thousand radiance maps may be displayed and several hundred spatially integrated signatures may be requested. Our approach to emissivity and reflectance calculations allows the computation of the wavelength or bandpass quantities separately from the angular portions. The wavelength dependent terms are pre-computed and the graphics rendering library produces real-time display of the target IR image as the observer-target-source geometry changes. The organization of the calculations is critical to successful real-time implementation. The goal is to complete preprocessing of the wavelength or bandpass quantities in the time that is typical for single signature calculations, then to compute hundreds of signatures in real time. The QUID model also uses pre-calculated atmospheric simulations, which are generated with the MODTRAN<sup>TM6</sup> radiation transport model, to incorporate solar radiance, atmospheric transmission, thermal emission, scattering, and clutter (clouds, weather, etc.) effects into the simulation.

Under the current effort, the source code of QUID has been recently rewritten in object-oriented C++ in order to take advantage of open-source libraries for graphics and windowing/graphical user interface functions. Some new capabilities introduced with this version include:

- Support for user definable target trajectories to simulate dynamic threat scenarios,
- Modeling of aerodynamic heating and solar shadowing effects,
- An upgraded plume model based on a pre-calculated database of high-fidelity flowfield and radiometric signature calculations, and
- Functions to analyze radiometric intensity in a selectable band of interest for a target as a function of range, time, and aspect angle of attack.

This version of QUID is cross-compatible with Linux, Windows (XP or 2000) and SGI platforms. A comprehensive graphical user-interface (GUI), designed with the wxWidgets<sup>7</sup> GUI framework, allows the user to interactively control the parameters of a simulation. For the graphics-rendering functions, QUID draws on the OpenSceneGraph<sup>8</sup> (OSG)

library, an advanced 3-D graphics toolkit for the development of high performance graphics applications in the fields of visual simulation, games, virtual reality, scientific visualization and modeling. The OSG library is based around the OpenGL<sup>9</sup> standard and offers the performance benefits of other established 3-D graphics toolkits such as Performer<sup>10</sup> (Silicon Graphics) and Vega Prime<sup>11</sup> (MultiGen-Paradigm), but is also open-source and cross-platform compatible.

## 2.1 Spectral Radiance Model

The IR signature of a target is composed of five basic signature components including:

- Thermal surface emissions,
- Scattered solar radiation,
- Scattered earthshine,
- Scattered skyshine, and
- Exhaust plume emission from hot molecular or particular species.

The scattering of solar radiation, earthshine and skyshine depends on the BRDF of a surface, which completely defines the optical properties of opaque surfaces. The BRDF is defined as the surface reflectance for a given wavelength ( $\lambda$ ), angles of incidence ( $\theta_i, \phi_i$ ) and angles of reflectance ( $\theta_r, \phi_r$ ). The angles are measured from the surface normal,  $\mathbf{n}$ , to the observer and source vector,  $\mathbf{o}$  and  $\mathbf{s}$ , respectively. The BRDF is written in Equation 1 as a sum of terms that are factored into wavelength,  $\rho'_k(\lambda)$ , and angular,  $F'_k(\theta_i, \phi_i; \theta_r, \phi_r)$ , components. This representation of the BRDF is quite general and includes standard models such as the Sandford-Robertson (SR) model used in SPIRITS. The BRDF can be written as

$$f_r(\lambda; \theta_i, \phi_i; \theta_r, \phi_r) = \sum_k \rho'_k(\lambda) / F'_k(\theta_i, \phi_i; \theta_r, \phi_r) \cdot \quad (1)$$

When a surface shows no preferential direction, or striae, the number of angles required to define the BRDF is reduced from four to three. The BRDF can also be written in terms of the glint angle,  $\alpha$ , and a scattering angle,  $\chi_s$ , see Figure 1. The glint vector,  $\mathbf{g}$ , is given by

$$\mathbf{g} = (\mathbf{o} + \mathbf{s}) / \sqrt{2(1 + \mathbf{o} \cdot \mathbf{s})} \quad (2)$$

The glint angle,  $\alpha$ , is defined as the angle between  $\mathbf{g}$  and the surface normal. It is given by

$$\cos \alpha = \mathbf{g} \cdot \mathbf{n} \quad (3)$$

where  $\mathbf{n}$  is the direction of the surface normal. The scattering angle,  $\chi_s$ , is the angle between the glint vector,  $\mathbf{g}$ , and source vector,  $\mathbf{s}$ . Note that  $\alpha=0$  corresponds to maximum specular reflection. The BRDF can be written in terms of the glint and scattering angles as

$$f_r(\lambda; \theta, \alpha, \chi_s) = \sum_k \rho_k(\lambda) F_k(\alpha, \chi_s) \quad (4)$$

QUID can use BRDF representations as given in Equation 1 or 4. During a calculation the  $\rho_k(\lambda)$  terms are pre-computed for a grid of observer-target ranges and a given bandpass. The  $\rho_k(\lambda)$  terms include all of the atmospheric transmission effects that vary with range and altitude, but do not vary with target orientation. The angular components in Equation 1 and 4 are then calculated each time the target-observer geometry changes.

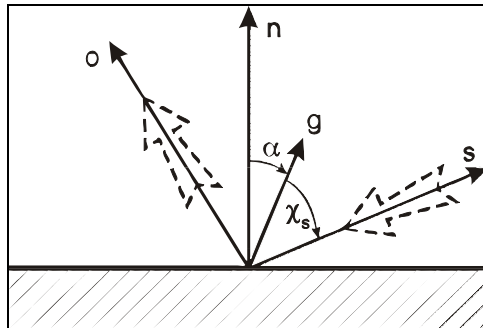


**Figure 1.** Angles for scattering by a surface element.

## 2.1 Directional emissivity

The directional emissivity can be obtained from the measured total reflectance, assuming opaque surfaces. It has been observed<sup>5</sup> that the directional emissivity can be very well represented with angular and wavelength-dependent factors. This factorization assumption is used in SPIRITS target modules. The emissivity is taken as a product of a wavelength dependent function, the spectral emissivity,  $\varepsilon_\lambda$ , and the angular falloff function,  $g(\theta_o)$ , where  $\theta_o$  is the angle between the observer and the surface normal. This relationship can be written as

$$\varepsilon(\lambda, \theta_o) = \varepsilon_\lambda g(\theta_o) \cdot \quad (5)$$

The evaluation of the contribution to the spectral apparent radiance of a target from thermal emission is found by the simple formula

$$L_\lambda = \sum_i^N \{ \varepsilon_\lambda B(\lambda, T_i) \tau(\lambda) \} g(\theta_o) a_i(\theta_i) \quad (6)$$

where  $B(\lambda, T_i)$  is the black body function for the  $i$ th surface,  $a_i(\theta_i)$  is its projected area and  $\tau(\lambda)$  is the atmospheric transmittance and the sum is over all target facets. The equivalent in-band apparent radiance requires an integration of  $L_\lambda$  over the desired bandpass. The angular falloff functions and the projected areas in Equation 6 can be evaluated in real-time.

## 2.2 Solar reflectance

The factorization method applied to direct reflected solar irradiance from a surface is

$$L_\lambda = S(\lambda) \rho(\lambda, \Theta_s, \Phi_s, \Theta_o, \Phi_o) \cos(\Theta_s) a(\Theta_o) \quad (7)$$

where  $S(\lambda)$  is the L-path transmitted solar irradiance,  $\rho$  is the BRDF and  $a(\Theta_o)$  is the unobscured projected surface area. The BRDF can be expanded, as in equation 4, leading to three terms

$$\pi L_\lambda = \{ S(\lambda) \} a(\Theta_o) \cos(\Theta_s) - \{ S(\lambda) \varepsilon_\lambda \} a(\Theta_o) \cos(\Theta_s) g(\Theta_o) g(\Theta_s) + \{ S(\lambda) \rho_\lambda \} a(\Theta_o) \frac{h(\alpha) - H(\Theta_s) H(\Theta_o)}{\cos(\Theta_o)} \cdot \quad (8)$$

The above terms in brackets are only functions of wavelength and not functions of observer-object-solar angles. QUID uses preprocessed values of the quantities in brackets and bandpass values of the quantities for spectral and inband signatures and radiance maps. The angular terms are evaluated on the fly as object orientation changes in the QUID simulation. It is the use of Equations 6 and 8 that allows the real-time evaluation of target inband and spectral signatures in QUID model.

## 3. TARGET MODELING AND SIMULATION

QUID imports wire models of the subject threat and calculates radiometric properties based on emissivity, temperature, and environmental effects (aero-heating, shading). The plume model, if any, is imported as a separate structure and joined to the hardbody wireframe. Spectral band inputs for are user selected dynamically within the GUI. The co-joined model can then be run thru the user trajectory with atmospheric attenuation folded in for presentation to the viewer or scene projector. Radiometric functions of range, field-of-view (FOV), atmospheric attenuation and graphics representation / presentation are of primary importance in the realization of dynamic scenario infrared scene projection.

Figure 2 shows a series of images generated by QUID for a uniformly painted aircraft as the spectral region of interest is varied from the LWIR to the visible. These images include thermal emission, flat surface direct solar scattering and atmospheric attenuation effects, but do not include an engine plume model. Notice that the thermal emission from the hot engine parts dominate the signature in the LWIR and the solar glints off the aircraft are the brightest radiance sources in the visible. The solar glint model is essential in the correct simulation of spectral glints from target surfaces.

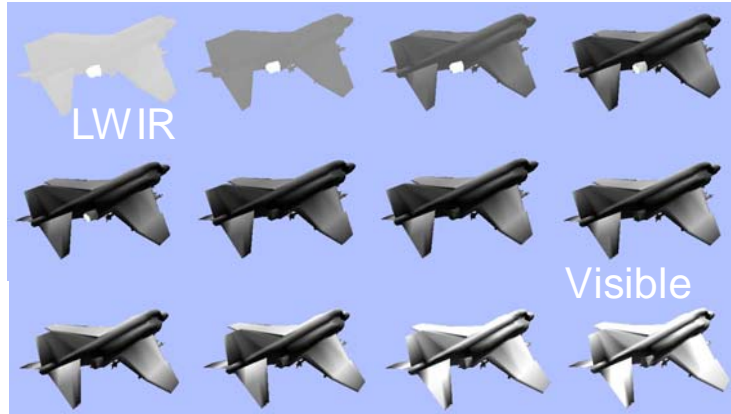


**Figure 2.** Examples of multispectral bandpass radiance images of an aircraft generated for LWIR (upper left), MWIR, SWIR, NIR, and VIS (lower right) regions.

QUID currently creates a realization of engine plumes for a given aspect angle, missile/aircraft velocity, and altitude from a large database of line-of-sight radiometric calculations. The calculations are performed on a fine grid, which results in a faceted representation of the transmissive/emissive plume with over 500 elements where the spectral emissivity and transmissivity of each vertex is stored. This level of detail provides a very high-fidelity signature calculation, but can hinder the obtainable frame rate. Some options for maximizing plume model fidelity and simulation frame rates using textures and/or multiple levels of detail to achieve accurate, real-time scene generation are under investigation.

In the MWIR region, the dominant sources of a missile signature are hot particulate and molecular species emission within the plume. Figure 3 depicts a detailed MWIR QUID signature calculation for a broadside view of a sidewinder anti-aircraft missile, shown in a false-color spectrum to contrast the range of intensities from the plume and hardbody. The pre-calculated plume data for this model was created using the current version of the Standardized Plume Flowfield Model<sup>12</sup> (SPF), SPF-III, and the Standard Plume Ultraviolet Radiation Code (SPURC): Low Altitude (LA)<sup>13</sup>, a JANNAF (Joint Army-Navy-NASA-Air Force) code. SSI has upgraded the radiation-transport database in SPURC to include additional species and greater spectral coverage, which may be important for representing some threat systems.

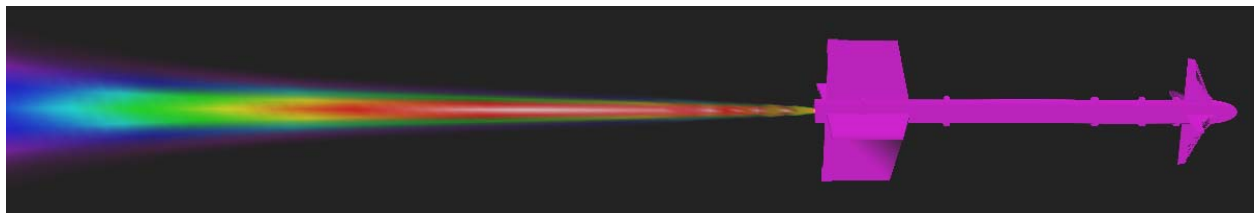


**Figure 3.** A MWIR QUID signature calculation of a sidewinder missile, shown in a synthetic color-temperature spectrum. Smaller radiance values are represented by colder colors (purple/blue), with larger values appearing as warmer colors (red/white).

The missile hardbody can influence the signature in more than one way, principally by obscuring some portion of the plume from the detection system. Under certain aspect angles, this obscuration can significantly attenuate the total signature. Figure 4, which depicts this effect, contains data from a QUID signature calculation for an approaching air-to-air missile trajectory recorded with a simulated 100 Hz sampling rate. For the nearly nose-on view of the missile, the total radiant intensity closely follows changes in the aspect angle because the strongest emission sources are hot  $H_2O$  and  $CO_2$  species near the center-axis of the plume. When considered as a MW source, emission from most metallic surfaces is negligible, so the only hardbody contributions to the signature worth noting arise from the reflections of the solar irradiance and plume emission. The solar reflection term is already treated in QUID, though plume and hot surface reflections are not currently supported. Spectral signatures of the same target as a function of aspect angle are shown in Figure 5. During any point in the QUID simulation, the trajectory may be frozen and a spectral integration performed on the object and output to file.

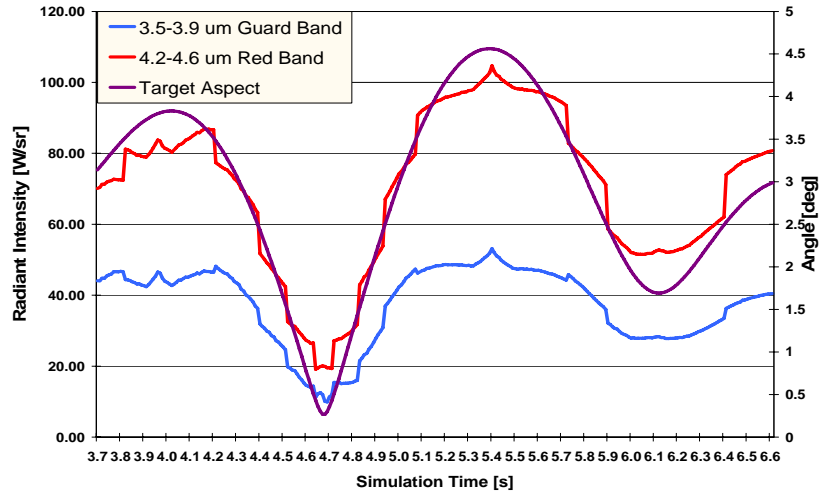


**Figure 4.** A time-dependent radiance signature of a missile in flight, integrated for two bands. The total radiant intensity (red and blue) closely follows the missile aspect angle (purple), due to obscuration of the plume by the missile hardbody.

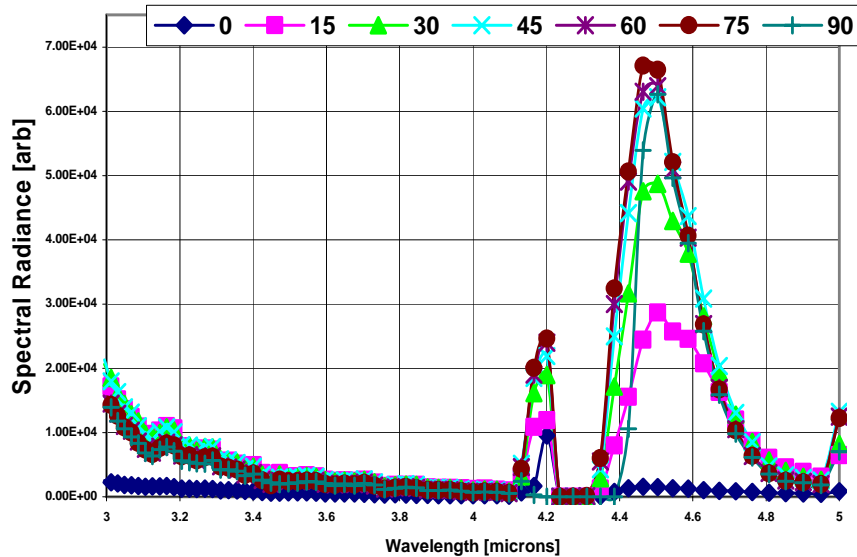


**Figure 5.** Spectral radiance signatures (MWIR) of the same missile for a series of aspect angles.

### 3.1 Scaling and range test

For a simulated model to be correctly described in scene projection over a range of simulation distances, from a point-source object to zero-range baseline, the radiant intensity of the object must be conserved after accounting for atmospheric transmission and throughput. As the range to a represented threat changes, the subtended angle and solid angle grows inversely as approximately the square of the distance. The source radiance per solid angle remains constant in the sensor direction, but the number of pixels available to represent that radiance diminishes to a point source and fine features of the model are lost. In simulation, the source propagated (virtual) radiance is converted to intensity at the projector plane, and then re-propagated (as energy) to the sensor under test; but the source radiance must remain invariant.

Real world objects are spatially integrated in irradiance prior to interception by the sensor aperture. In addition, changes in gain or FOV of the sensor system do not alter the natural object radiance yet in general, the problem of simulation has historically been approached from the pixelated point of view; i.e. an object's signature can be modeled and rendered point-by-point or polygon-by-polygon and presented to the viewer. Intensity can be increased by electronic magnification, and level of detail expanded by FOV. In fact, neither of these operations affects a real world object and in the truest stimulation that would also hold true. Zoom window over sampling (ZAA)<sup>14</sup> is one demonstrated method to increase object sampled polygons per pixel and applying radiance conservation in an SGI based rendering system. Given an infinite number of polygons per pixel, this would approximate realistic scenes and objects. However, there are always limitations on both polygon and pixel counts due to computational overhead and system throughput. This method still relies on sampled pixels from polygon rendered objects and so is dependent on the object sample size. In that reference, projected pixel area instead of source area, is used. QUID signatures are also calculated based on the projected area of object surfaces, using a method that combines emissive and projected area angular falloff in an efficient algorithm.<sup>2</sup>

Rendered objects that do not fill either the sensor FOV or one instantaneous FOV (IFOV) (which point sources by definition do not) violate invariance of radiance by under-sampling the object. The radiant value is computed from the sensor footprint on the object; therefore, if the apparent distance to the object changes it may not have the same simulated radiance because the number of sampled polygons per pixel has changed. Zoom sampling increases the effective number of pixels on target by using sub-pixel sampling windows. Totals are accumulated transferring the radiance value to the selected pixel or divides radiance into that and several near-by pixels. Pixels here are ultimately either emitter elements or sensor elements, no distinction has been (or needs to be) made in the front stage.

Williams *et al.*, Super Sub Sampling (SSS)<sup>15</sup> method showed that the most precise OpenIR implementation is to use point primitives combined with area coverage anti-aliasing. The corrected method (CSSS) holds a buffered object with zero range area and radiance values (ground truth) for zoom window correction of computed simulation values and includes dynamic sub-sampling. Here, correction can be made to the losses in radiance as pixels are culled from the graphics pipeline in the graphics transformation; and accounting for the differences in projected solid angle of each part of the object over the aperture by conservation of throughput  $H = A \Omega$  (area times projected solid angle).

However, shadowing effects for real complex structures other than simple flat plates will complicate the CSSS method. As an object moves further in distance, parts may become shaded by wings, fins, etc. cutting off radiant parts which are seen close up and changing the spectral and radiometric signatures. Portions of the radiance which are present near field may not be in the far-field line of sight, for example, a fin shielding an exhaust port; therefore a ground truth image at each range and orientation must be used for comparison calculations, negating some of the advantages of the corrected reference image method. QUID features OpenGL hidden surface calculations based on LOS which could be used in combination with a corrected SSS method to correct both shading and pixel / radiance loss effects.

### 3.2 Radiometry

Radiant energy transfer rather than imaging criteria will be discussed in this section with both near and far field radiation. The standard treatment regarding infrared scene projector output radiance and definition of effective blackbody temperature is given by Williams<sup>16</sup> for a generic, far field scene delivered to the entrance pupil of an imaging system under test. Flynn, Marlow, Sisko and Thompson<sup>17</sup> have elegantly shown that integrating over the radiance of the target gives the aperture irradiance, independent of system blur functions. This is consequence of the conservation of throughput and radiance invariance.

The treatment shown in Figure 6 follows Nicodemus, *et al.*,<sup>18</sup> with  $R$  for range,  $L$  for radiance, and  $H$  for throughput. For a near field reference object, each polygon of the virtual object area may be considered a near small source for Jones method of calibration<sup>19</sup> of radiance with the field stop coincident with the aperture stop. Even if the entire object fills the FOV, it is still treated as being composed of many smaller, non-uniform surfaces. The graphics transform converts virtual world radiance quantities to mapped values of thermal energy at the emitter array, and is otherwise completely transparent, isotropic and of infinite extent.

Throughput describes the geometric factors that are invariant in radiation transfer from one surface (or point) to another. For the near object, each part of the object within an IFOV solid angle must be corrected by the cosine of the surface normal to the direction of the sensor and the cosine of the angle from emitter to object element. An element of throughput is therefore written as

$$dH = dA_S \cos \theta_S dA_E \cos \theta_E / R^2 \quad (9)^{18}$$

and the total throughput is the integrated value over both source and emitter apertures,  $A_S$  and  $A_E$ , where each element has a different cosine obliquity factor.

The throughput, being purely geometrical, is invariant and conserved for all rays as long as the edge rays from the object pass thru all apertures and baffles, and without vignetting. The total flux,  $\Phi$ , or intensity at the projector aperture, is the integral over the projector aperture area  $A_E$  and over all projected solid angles subtended at the emitter plane by the source (projected area). In other words, since radiance is invariant and throughput conserved, if the source radiant object samples the emitter array, then that is equivalent to the end result of the graphics sampling and transformation on the image but without the under-sampling errors.

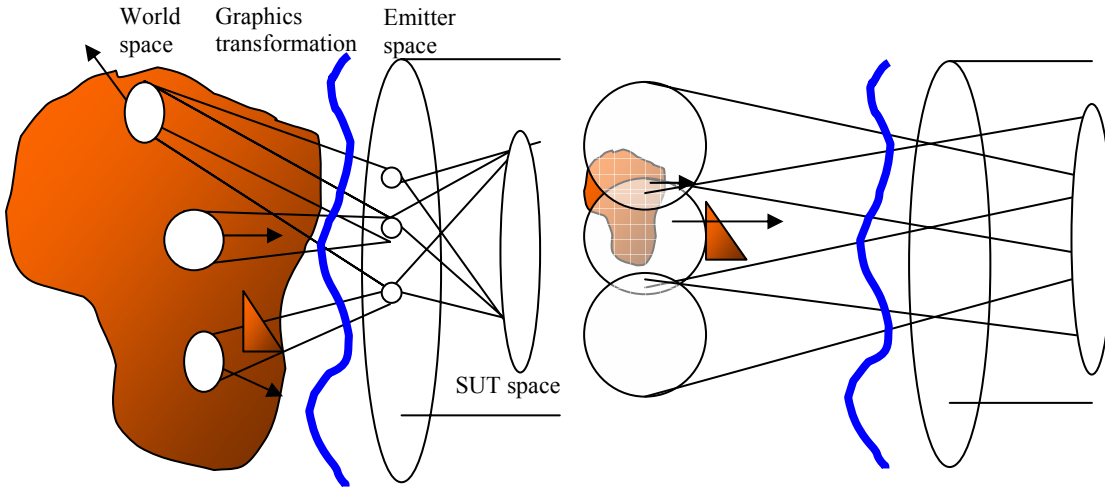


**Figure 6.** Energy transfer models of an infrared scene projector system shown for near-field (left) and far-field (right) cases.

For the far object, only rays with cosine factors approaching one are received at the projector plane, the range for all points on the object is essentially the same, and differences in angles for individual elements is negligible for the flat emitter array. Throughput can be formulated as the averaged value integrated over the aperture, or

$$H = A_E \Omega \quad (10)^{18}$$

where  $\Omega$  is the solid angle subtending the distant object as a whole. Collimator optics and refraction by the projector windows modifies the subtended image angle and throughput, but does not decrease the total received flux, except by transmission losses. For correction from the near field to far field cases, radiance is propagated along each ray, and scaled by the collimator transmission,  $\tau$ . Therefore, each discrete emitter element receives the same amount of radiance in the narrow beam of rays from a point on the source object, and the total is just the sum over the emitter array for the look angle. The throughput values for each emitter are approximately the same. The total propagated radiance is only dependant on the sum over the source object surface elements,  $L_s$ , in the direction to the emitter within the FOV, and not over pixels in the sensor or emitter or zoom window sub-sampling size. This invariance could be used to correct, simplify and speed calculation in the graphics and rendering stage in finding the total radiance:

$$\Phi = \frac{\tau}{R^2} \sum_E A_e \cos \theta_e \sum_S L_s A_s \cos \theta_s = \frac{\tau}{R^2} A_E \cos \theta_E \sum_S L_s A_s \cos \theta_s \quad (11)^{18}$$

For total propagated radiance, only the summation over the source object is needed (and only for elements of the object with  $\theta_s < 90$  deg.) even down to the un-resolved, point source resolution of the sensor. For each emitter element, the source object summation runs over the object polygons within each emitter projected solid angle (which requires computational power to determine which polygons to include); but the total radiance calculation need only run over the object once. Errors in sampling the source object polygons at insufficient resolution then summing over the samples lead to errors in the sum radiance value.

The total radiance emitted by the projector array is

$$L_E = \sum_E \frac{\Phi_e}{\Omega_e A_e \cos \theta_e}. \quad (12)^{18}$$

Generally, the final optical stage collimates the beam for imaging into the SUT at infinite conjugate; i.e. the object appears to originate from a far distance. For the distance object source and by the conservation of throughput and assuming separability, we can write as first approximation

$$H = A_S \Omega_S = A_E \Omega_E = A_C \Omega_C \quad (13)^{18}$$

and identify  $A_S \Omega_S$  with the source object to emitter array,  $A_C \Omega_C$  with the collimator to SUT and  $A_E \Omega_E$  with the emitter array to collimator with

$$\Omega_E = \frac{\pi}{4(F/\#)^2 + 1} \quad (14)$$

where  $F/\#$  is the projector emitter array output cone (lambertian radiation) defined by the collimator aperture corrected for refraction effects by any system windows. Here, a loss in throughput will translate into a loss in effective radiation temperature, the equivalent blackbody temperature over the wavelength band-pass for the amount of flux transmitted. Also, on a per pixel basis, all angular direction information from the scene under view has been lost by the radiance integration and emission of the simulated scene by the projector elements into a new radiation pattern.

Angle  $\theta_E$  the emitter angle, is associated with the platform. In scenarios where there is platform motion, the angle is variable when the end sensor is fixed and the look angle changes. On platforms where the end sensor can track, emitter angle will remain (generally) constant and aligned towards the object. These two modes have effect on the radiometry through the cosine factor.

One special case where source to emitter array sampling must be the preferred direction is in ultra-violet scene simulation, where scattering by the atmosphere occurs along the path. Sensors out of the LOS will receive scattered UV photons and so propagation is directional and cannot be separated from the basic radiance direction when integrating to find total irradiance at the emitter / sensor plane. Radiance is properly computed in the source to emitter direction only. UV scene projectors are also under development at ACETEF which will incorporate diffuse propagation algorithms.

In visual rendering<sup>20</sup>, the priority has been to optimize the information stimulus experience of the viewer, or sensor under test (SUT). Contrast level can be increased and intensity varied with gain and offset values. By decreasing the FOV of the display as the object moves away in range, the size and graphics calculated radiance of the object is held to a minimum of one display pixel and the radiance constant since the same number of pixels in the graphics buffer are available for rendering. In real world sense, these statements would not hold true. Object extent on the sensor plane is limited by diffraction, not pixel area; the object's true radiance is an integrated value based on projected area, not sampled pixel areas; and total flux at the sensor is determined by throughput reduced by path attenuation.

In IR scene projection and stimulation, the priority must be to present a naturally behaving object and make the graphics stage "transparent". The IR projector takes the world space virtual object and creates a photonic, radiometric signature map *of the propagated radiance* for output to the system under test, not an image or sensor response. This is the problem all simulations have grappled with in the move from visual rendering to physics based rendering. The key here is to first spatially integrate the object in the projector / emitter plane, rather than sample in the object plane. That way, at least a real world flow of events, if not complete replication is achieved.

Source data, even from live-fire shots, is supplied as zero range corrected radiance, and is spatially digitized requiring integration and range transformation based on viewing geometry. ACETEF plans include working with the Missile and Space Information Center (MSIC), Huntsville, Ala., in evaluation of full spectra model data based on live-fire events data with latest data format structures, E-MSIG, which will allow graphics rendering to be supplied for the necessary range corrections, eventually in real-time to 400 Hz. By identifying the nature of this problem, ACETEF hopes to carry QUID simulation to this next level.

#### 4. RADIOMETRIC SCALING TESTS

The following set of test simulations were carried out to evaluate the radiometric accuracy of QUID signatures as a target undergoes motion. The atmospheric attenuation can be turned on and off to quantify that effect or eliminate it from consideration. The sensor FOV also can be varied to hold the effective area of an object constant or fixed to view the effect of lost pixels with range. In fielded systems, the FOV generally is wide for warning sensors and narrow, often with dual fields, for fine tracking systems. For a reference baseline, atmospheric attenuation is turned off, and the effective area of the target held constant with distance. A second baseline includes atmospheric attenuation, but holds the display area constant. Four cases are thus generated as a function of range, as shown in Figure 7. The threat object is at 45 degrees aspect, with range varying between 0.5 to 40 km.

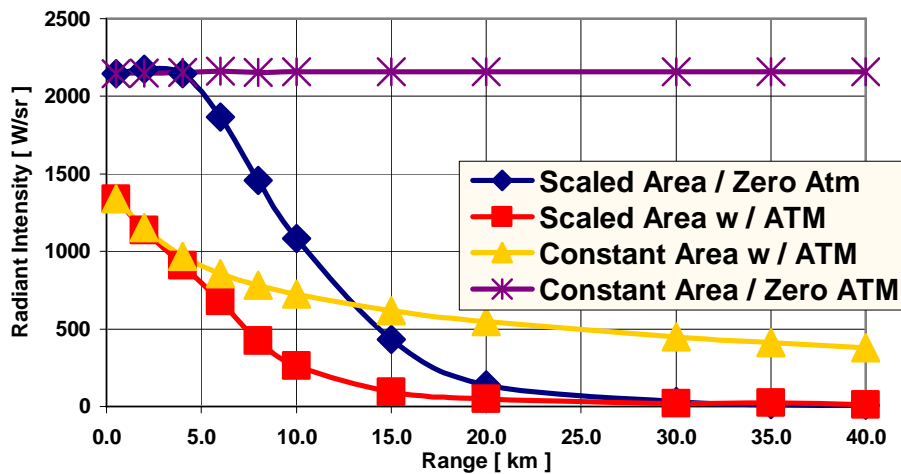


Figure 7. Range dependence of pixel and atmospheric effects on model radiant intensity.

A variable to account for lost signature information, Tau, represents attenuation factors which are the ratio of the broadband radiance values with and without one variable held constant. Shown in Figure 8, Tau (pixel) is introduced as the scaling factor of the simulated band averaged radiance (3- 5 microns) as a function of range with and without atmospheric attenuation. Tau (atm) is the computed total attenuation of the hard-body and plume radiance with a variable or fixed apparent target area. Note the properties considered in two of the cases are ratios to fixed area or zero atmosphere baselines, while Tau (atm with scaled area) is a ratio of one variable (atm) to another (pixel area), which scales inversely with range. As the projected area goes to zero, this last ratio becomes undefined at infinity (actually much shorter ~ 15 km begins to diverge). Range dependence of  $1/R^2$  (normalized to 0.5 km in Figure 8) on the propagated radiance is then treated as a propagation factor arising from the throughput equation.

The pixel attenuation for this object is seen to hold well out to 5 km, then decreases. If the pixel attenuation follows the range dependence then the propagated radiance will fall off immediately; however it does appear to approach the  $1/R^2$  dependency after 5 km. The atmospheric attenuation of the object radiance for the constant area case is as expected from the MODTRAN model implemented in QUID, also holding well out to 5 km for the scaled area case in this example. Pixel attenuation is dependant on the resolution of the graphics, and on constrictions in the graphics pipes used to render data and on the nature of the object itself.

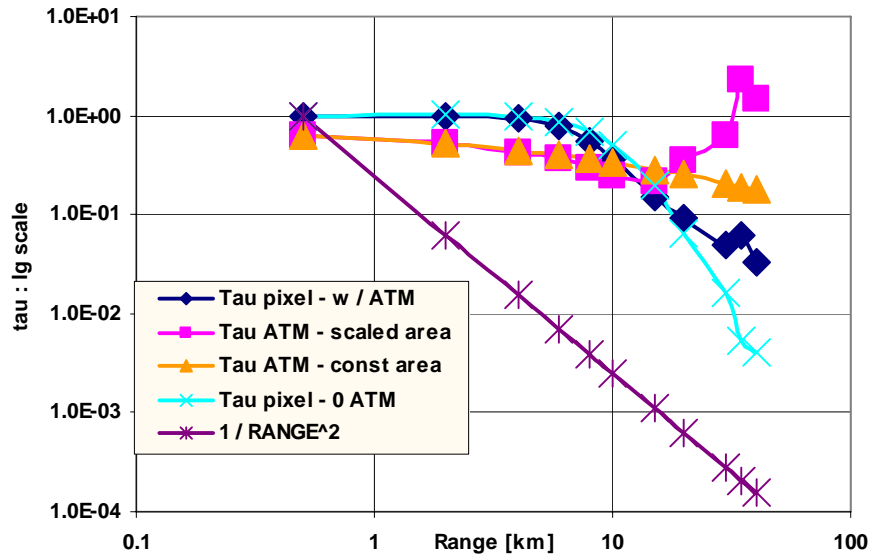


Figure 8. Calculated radiance attenuation factors from atmospheric and pixel loss.

## 5. FUTURE WORK

Future versions of QUID may treat flow field curvature of the plume, additional flyout stages and time varying plume shapes. The look angle treats the target body as a point, but may later be defined to the target radiometric centroid. Relative sensor / platform motion could be built into other trajectories, and a future QUID version may add independent platform and sensor motions, as well as sensor effects (QUID currently has a user input for background radiometric noise figure) and will calibrate pixel attenuation of intensity to follow the expected attenuation with range. Future versions may run real-time projection as computational speed improvements are explored. Zoom and Corrected Super Sub-Sampling methodologies (GPU ZAA<sup>21</sup> and CSSS) also will be explored to increase fidelity.

## REFERENCES

1. T. Perkins, and R.L. Sundberg, "QUID User's Manual -Version 3.0," Prepared for NAWCAD ATL Ranges & Facilities, 48150 Shaw Road, Unit 5, Patuxent River, MD 20670, Under Contract No. N00421-03-C-0078, (June 2005).
2. R.L. Sundberg, J. Gruninger, M. Nosek, J. Burks, and E. Fontaine, "Quick image display (QUID) model for rapid real-time target imagery and spectral signatures," Proc. SPIE, 3084, 272, (1997).
3. R.L. Sundberg, and J. Gruninger, "Quick Image Display (QUID) Model for SPIRITS," 1998 JANNAF SPIRITS User Group Meeting, NASA Kennedy Space Center, FL (1998).
4. B.P. Sandford, and D.C. Robertson, "SPIRITS Module for the F-16C," PL-TR-97-2071, Hanscom AFB, MA (1997).
5. See <http://www.multigenparadigm.com/products/standards/openflight/> for more information on the OpenFlight standard.
6. A. Berk, G.P. Anderson, P.K. Acharya, L.S. Bernstein, L. Muratov, J. Lee, M. Fox, S.M. Adler-Golden, J.H. Chetwynd, M.L. Hoke, R.B. Lockwood, T.W. Cooley, and P.E. Lewis, "MODTRAN5: A Reformulated Atmospheric Band Model with Auxiliary Species and Practical Multiple Scattering Options," SPIE Proceedings Vol. 5425, Orlando, FL (March 2004).
7. See <http://www.wxwindows.org/> for more information on the wxWidgets library.
8. See <http://www.openscenegraph.org/> for more information on the OpenSceneGraph library.
9. OpenGL Architecture Review Board, OpenGL, Reference Manual, Addison-Wesley, Reading, MA (1993).
10. See <http://www.sgi.com/products/software/performer/> for more information on SGI Performer.
11. See [http://www.multigenparadigm.com/products/runtime/vega\\_prime/](http://www.multigenparadigm.com/products/runtime/vega_prime/) for more information on the Vega Prime system.

12. M.W. Taylor, and H.S. Pergament, "Standardized Plume Flowfield Model, SPF-III, Vol. 1 Model Formulation and Numerical Algorithms," PST TR-39-I (February 1998).
13. R.M. Gutowski, and P. Markarian, "Standard Plume Ultraviolet Radiation Code (SPURC): Low Altitude (LA) 1.3 Users Manual," PL-TR-97-3018 (September 1998).
14. E.M. Olsen, Garbo, D.L., Crow, D. R., and C.F. Coker, "Rendering energy conservative scenes in real-time," Proc. of the Technologies for Synthetic Environments: Hardware-in-the-loop Testing II," SPIE Vol. 3084, pp. 250-259, (1997).
15. T.G. Sills, and Williams, O. M., "Aliasing and scintillation reduction in real-time computer graphics," Proc. of the Technologies for Synthetic Environments: Hardware-in-the-loop Testing VIII," SPIE Vol. 5092, pp. 247-258, (2003).
16. O.M. Williams, "Infrared projector effective blackbody temperature," Optical Engineering," Jan. 1994, Vol. 33 No. 1, pp. 230- 236.
17. D.S. Flynn, Marlow, S. A., Sisko, R. B., and Thompson, R. A., "Accuracy of Aperture irradiances from a resistor-array projection system," Proc. of the Technologies for Synthetic Environments: Hardware-in-the-loop Testing X," SPIE Vol. 5785, pp. 112-123, (2005).
18. F. Nicodemus, ed., "NIST Self-Study Manual on Optical Radiation Measurements," National Institute of Standards and Technology, 1977 – 1985, CD-ROM version, ch. 2, pp. 10 – 44.and appendix 2, pp. 62 – 81.
19. G.J. Zissis, "The Infrared & Electro-Optical Systems Handbook," Vol. 1, ch. 4, Environmental Research Institute of Michigan, 1993, pp. 326-334.
20. NVIDIA Technical Brief, "Transform and Lighting," NVIDIA Corp.
21. E.M. Olsen and T.P. Bergin, "Using programmable graphics to improve zoom window anti-aliasing," Proc. of the Technologies for Synthetic Environments: Hardware-in-the-loop Testing IX," SPIE vol. 5408, pp. 164 – 172, (2004).